Geophysical Research Letters

RESEARCH LETTER
10.1029/2020GL088946

Key Points:

- ~15.9 million satellite observations over 35 years show USA rivers (>60 m wide) are dominantly yellow and green in color
- River color has three distinct seasonal patterns that are synchronous with flow regimes
- River color significantly changed over the last three decades in one third of large US rivers

Supporting Information:

- Supporting Information S1

Correspondence:
J. R. Gardner,
gardner.john@pitt.edu

Citation:
Gardner, J. R., Yang, X., Topp, S. N., Ross, M. R.. V., Altenau, E. H., & Pavelsky, T. M. (2021). The color of rivers. *Geophysical Research Letters*, *48*, e2020GL088946. https://doi.org/10.1029/2020GL088946

Received 21 MAY 2020
Accepted 19 NOV 2020

© 2020. American Geophysical Union. All Rights Reserved.

The Color of Rivers

John R. Gardner[1,2], Xiao Yang[1], Simon N. Topp[1], Matthew R. V. Ross[3], Elizabeth H. Altenau[1], and Tamlin M. Pavelsky[1]

[1]Department of Geological Sciences, University of North Carolina at Chapel Hill, Chapel Hill, NC, USA, [2]Department of Geology and Environmental Science, University of Pittsburgh, Pittsburgh, PA, USA, [3]Department of Ecosystem Science and Sustainability, Colorado State University, Fort Collins, CO, USA

Abstract Rivers are among the most imperiled ecosystems globally, yet we do not have broad-scale understanding of their changing ecology because most are rarely sampled. Water color, as perceived by the human eye, is an integrative measure of water quality directly observed by satellites. We examined patterns in river color between 1984 and 2018 by building a remote sensing database of surface reflectance, RiverSR, extracted from 234,727 Landsat images covering 108,000 kilometers of rivers > 60 m wide in the contiguous USA. We found 1) broad regional patterns in river color, with 56% of observations dominantly yellow and 38% dominantly green; 2) river color has three distinct seasonal patterns that were synchronous with flow regimes; 3) one third of rivers had significant color shifts over the last 35 years. RiverSR provides the first map of river color and new insights into macrosystems ecology of rivers.

Plain Language Summary Rivers can appear different colors such as blues, greens, browns, and yellows. Water color is linked to water quality and can be related to the amount of sediment, algae, and dissolved organic carbon in water. Humans can therefore discern waters' suitability for use with our eyes. While we know many rivers are impaired globally, often due to poor water quality, the color of rivers has not been widely measured to investigate changes through space and time. Satellites act as "eyes in the sky" and regularly observe earth's large rivers. Using satellite remote sensing records from 1984 to 2018, we measured the color of rivers across the USA. We found that large rivers have distinct seasonal patterns in color that change with river flow, and that the dominant color in one third of rivers has significantly changed. Observations of water color can pinpoint rivers undergoing rapid environmental change and work toward continental-scale understanding of rivers.

1. Introduction

Rivers are among the most degraded ecosystems on earth (Best, 2019). Water quality is impaired due to human activities such as agriculture and urbanization (Foley et al., 2005; Meybeck et al., 1990), and currently only 23% of earth's largest rivers flow uninterrupted to the ocean (Grill et al., 2019; Nilsson et al., 2005). Because large rivers integrate millions of kilometers of land area, understanding rivers and their impairments is inherently macroscale: both distant and local impacts generate the patterns we observe (Heffernan et al., 2014; McCluney et al., 2014). There is a profound need for integrative water quality measurements that are spatially explicit and globally scalable, as local and global changes impairing Earth's rivers cannot be fully understood using sparse, ground-based measurements (Stanley et al., 2019; Stets et al., 2020).

Remote sensing enables spatially explicit, global observations of large rivers (Palmer et al., 2015). Satellite missions, such as the joint NASA/USGS Landsat mission, have been used for decades to measure river and lake water quality (Brezonik et al., 2005; Carpenter & Carpenter, 1983). However, measuring water quality at continental to global scales remains challenging over inland waters due to optical complexity, or the presence of multiple water quality constituents (Ross et al., 2019; Topp et al., 2020). The three main constituents are chlorophyll-*a* (chl-*a*), suspended sediment, and colored dissolved organic matter (CDOM) (Davies-Colley et al., 2003; Ritchie et al., 2003). These water quality constituents are ecologically important, control light availability for photosynthesis and photodegradation, and together determine the color of water which is an integrative measure of water quality (Cory et al., 2014; Davies-Colley & Close, 1990; J. Julian et al., 2008).

Water color, as perceived by the human eye, is also an intuitive and broadly applicable water measurement (Lehmann et al., 2018). It is intuitive since it is based on human perception of color, and people often

discern water's suitability for consumption, recreation, and aesthetic value based on water color (Smith & Davies-Colley, 1992; West et al., 2016). Color is broadly applicable because it does not require knowledge of the inherent optical properties of water and can be directly measured by any optical imager with bands in the visible spectrum (Giardino et al., 2019; Van der Woerd & Wernand, 2018). Lastly, water color is one of the oldest measurements of water quality (Forel, 1895; Hutchinson, 1957) and is widely used in community science campaigns (https://www.eyeonwater.org/).

When combined with satellite remote sensing, water color may inform macrosystems ecology in rivers. Large river systems are excellent candidates for macroscale analysis given their directional connectivity and integration of landscapes (Fuller et al., 2015; McCluney et al., 2014; Poole, 2002). In practice, macrosystems ecology of inland waters has largely relied on synthesis of point-based field measurements (Butman & Raymond, 2011; Woodward et al., 2012). While spatial data of water presence are now widely available (Allen & Pavelsky, 2018; Pekel et al., 2016), there is a lack of spatial data of water properties in rivers to ask macroscale questions.

To address this gap, we examined macroscale patterns in river color by developing a database of river surface reflectance and color (RiverSR). Building upon existing data products and algorithms (Ross et al., 2019; Yang et al., 2019), we automated the extraction of surface reflectance (R_s) using the cloud-based geospatial analysis platform Google Earth Engine (GEE) (Gorelick et al., 2017) over all rivers > 60 m wide in the contiguous USA (CONUS) across Landsat 5, 7, and 8 from 1984 to 2018. Our goal was to provide an initial description of broad trends and patterns in river color. We asked 1) What is the most common color of rivers? 2) What are the seasonal patterns in river color? 3) How has river color changed over the last 35 years?

2. Materials and Methods

2.1. Satellite Imagery

USGS Landsat Surface Reflectance Tier 1 products (T1-SR) collected by Landsat 5 Thematic Mapper (TM), Landsat 7 Enhanced Thematic Mapper Plus (ETM+), and Landsat 8 Operational Land Imager (OLI) available in the Earth Engine Data Catalog were used to measure a time series of surface water color—expressed as dominant wavelength (see Section 2.2)—for 33,944 river reaches across CONUS from 1984 to 2018 (Figure S1). Although Landsat was intended for remote sensing of terrestrial surfaces, a large body of work has demonstrated that Landsat can accurately measure inland water quality in smaller waterbodies given a spatial resolution of 30 m (Brezonik et al., 2005; Carpenter & Carpenter, 1983; Giardino et al., 2001; Griffin et al., 2018; Kuhn et al., 2019; Mertes et al., 1993; Olmanson et al., 2008; Ritchie & Cooper, 1988) and cloud-free observations capture a wide range of flow conditions in rivers > 60 m wide (Allen et al., 2020). Landsat T1-SR products derived from Landsat 5 and 7 are atmospherically corrected using the Landsat Ecosystem Disturbance Adaptive Processing System (LEDAPS) and T1-SR derived from Landsat 8 uses the Landsat Surface Reflectance Code (LaSRC) (Claverie et al., 2015; Schmidt et al., 2013; Vermote et al., 2016). To account for minor differences in the spectral response of sensors used across Landsat missions, we corrected R_s from Landsat 5 and 8 to match Landsat 7, an approach similar to those used in terrestrial remote sensing (Roy et al., 2016). Using all R_s measurements during periods of overlap over the same locations between Landsat 5-7 (1999–2012) and 7-8 (2013–2018), we used a second-order polynomial regression of the 1%–99% percentiles of R_s within each band between sensors (5 to 7 and 8 to 7). Correcting Landsat 5 and 8 created more harmonized R_s time series (Figures S2 S3, Table S1).

Extracting R_s over rivers is challenging due to their small size relative to image resolution (e.g., 30 m for Landsat) and fluctuating position and size over time (Tomsett & Leyland, 2019). We automated R_s extraction using GEE via its python (v3.7.3) API (ee package v1.7.9) accounting for fluctuating river position, size, topographic shadows, clouds, and obstructions. First, to capture potential river migration and size fluctuations, we truncated a shapefile of National Hydrography Database (NHDplusV2) centerlines (Moore & Dewald, 2016) to the footprint of large Landsat visible rivers using Global River Widths from Landsat (GRWL) centerlines (Allen & Pavelsky, 2018), and created nonoverlapping polygons for NHDplusV2 reaches (median length = 2 km). The Dynamic Surface Water Extent (DSWE) algorithm (Jones, 2015, 2019) was translated into GEE to a create a water mask for each Landsat image removing clouds/cloud shadow/ice

influenced pixels according to the pixel quality assessment (pixel_qa) band derived from the FMask cloud detection algorithm (Foga et al., 2017; Zhu et al., 2015). We removed water pixels that were not part of the river channel by assessing each pixel's connectivity to the centerlines using cumulative cost mapping (Figure S4). Following water masking, the median surface reflectance in each band was calculated over the river reach water mask. Reaches with topographic shadow were removed by calculating hillshadow based on the MultiError-Removed Improved-Terrain (MERIT) digital elevation model (Yamazaki et al., 2019) and the position of the sun at the time of image capture, which was extracted from the Landsat metadata. Aggregating pixels to the reach scale served the dual purpose of building a product with river network topology as well as reducing data from 234,727 Landsat scenes to a manageable size for analysis. RiverSR data are publicly available and attachable to NHDplusV2 flowlines (see Acknowledgments).

2.2. Estimating Water Color

Using RiverSR, we quantified color using the dominant wavelength (λ_d) in the chromaticity color space. Chromaticity transforms RGB values into a human-perceived colorspace. λ_d therefore represents colors on the visible spectrum (in units of nm) rather than wavelengths of remote sensing reflectance spectra. λ_d is often binned into water color categories using the Forel-Ule scale (Pitarch et al., 2019; Wang et al., 2018). However, recent work used λ_d without binning to examine patterns and trends in water color across thousands of lakes in New Zealand and Italy (Giardino et al., 2019; Lehmann et al., 2018).

To calculate λ_d, R_s in the red, green, and blue bands are first converted into tristimulus values (X,Y,Z) that are mapped onto chromaticity coordinates (x,y,z) (Figure S5; Wang et al., 2014).

$$\begin{aligned} X &= 2.7689R + 1.7517G + 1.1302B \\ Y &= 1.0000R + 4.5907G + 0.0601B \\ Z &= 0.0565G + 5.5943B \end{aligned} \tag{1}$$

$$\begin{aligned} x &= \frac{X}{X+Y+Z} \\ y &= \frac{Y}{X+Y+Z} \\ z &= \frac{Z}{X+Y+Z} \end{aligned} \tag{2}$$

The hue angle (α) is calculated from the coordinates and transformed to λ_d by looking up the nearest wavelength to a given hue angle using the International Commission on Illumination tables (Wang et al., 2014).

$$\alpha = \left(\arctan 2\frac{x-0.33}{y-0.33}\right)\frac{180}{\pi} \tag{3}$$

We recognize the limitations of chromaticity. Chromaticity measures how the human eye perceives color and is known to be nonuniform and perceptually nonlinear (Hunt & Pointer, 2011). In other words, we may perceive two colors as slightly different, but they could have a similar λ_d. Furthermore, λ_d was calculated from three visible bands, and is therefore a spectrally coarse measure of color compared to hyperspectral measurements (Woerd & Wernand, 2015).

Satellite remote sensing of water also has limitations such as reliance on land-based atmospheric corrections, adjacency effects, sunglint, and riverbottom reflectance (Mouw et al., 2015; Zheng & DiGiacomo, 2017). Recent work shows that the Landsat 8 LaSRC atmospheric correction performs similarly to aquatic-based correction algorithms (e.g., SeaDAS and ACOLITE) for water quality applications (Kuhn

et al., 2019). Adjacency effects imposed by neighboring land and water pixels may be linked to environmental conditions, and some evidence suggests that adjacency effects in Landsat may be less pronounced over narrower inland waters such as rivers (Pahlevan et al., 2018). Sunglint may impact a small fraction of images, but λ_d will not change after sunglint correction since these methods typically multiply R_s in the visible bands by a constant (Hedley et al., 2005). Bottom reflectance may be contributing to the R_s signal, but likely only in clear rivers without vegetation since we remove vegetated water pixels using DSWE (Jones, 2015, 2019). To minimize the potential impact of adjacency and bottom effects, we repeated all analyses in Section 2.3 filtered to rivers >120 m wide using GRWL (Allen & Pavelsky, 2018; Frasson et al., 2019) and compared them to all rivers (>60 m). The results for all rivers versus rivers >120 m were similar, and our conclusions did not change (see Figures S6–S8 for the repeated analyses); therefore, we present the analysis of all rivers for completeness.

2.3. Analysis

Using RiverSR, we quantified the most common color for each river reach as the highest mode of the λ_d density distribution. For this analysis, we included only reaches with >10 observations collected over at least 15 years, totaling 93% (32,485) of RiverSR reaches. When referring to the absolute color, we divided λ_d into three broad color regions along the visible spectrum (yellow: ≥560 nm, green: 560–495 nm, blue: <495 nm; Lehman, 2018), see Figure S9 for example. We also quantified R_s magnitude (blue + green + red + nir/4) and averaged it over all observations at each reach to calculate the long-term mean R_s. According to NHDPlusV2, 5,306 reaches (16% by length; 16,400 km) of the river network were identified as connected lakes, and the remaining 27,179 reaches (84%; 87,996 km) were identified as rivers (Hill et al., 2018). While at least 25%–35% of these connected lakes are large storage reservoirs created by dams (Gardner et al., 2019), we refer to lakes and reservoirs as lakes for simplicity.

We classified long-term seasonal patterns in river color and evaluated their synchrony with long-term flow regimes quantified from United States Geological Survey (USGS) flow gauges. We restricted this analysis to river reaches with observations in all 12 months over at least 15 years (i.e., excluding rivers affected by seasonal snow/ice/clouds) including 55% (18,785) of reaches. We used dynamic time warping (dtw) to compare the temporal sequence of mean monthly z-normalized λ_d. To combine dtw with clustering, a dissimilarity matrix was calculated to group temporal sequences with the smallest distance between them or a similar temporal pattern. Barycenter averaging was used with complete linkage hierarchical clustering in the dtwClust package in R (Sarda-Espinosa et al., 2019). Similar methods were used to characterize river metabolic regimes (Savoy et al., 2019) as well as terrestrial vegetation phenology (Xue et al., 2014). The optimal number of seasonal patterns, or clusters, was identified by iterating from 2 to 8 clusters and calculating cluster validity indices (CVIs) (Arbelaitz et al., 2013). Internal CVIs quantify cluster purity and the optimum number was 2 or 3 clusters (Figure S10). Using flow gauges with >30 years of daily flow data between 1984 and 2018 ($n = 871$ sites, covering 4.6% of observed reaches), we calculated the proportion of annual flow that occurred within each month for each year, then calculated the median across all years to represent the median flow regime at each site (Scott et al., 2019). Sites were grouped according to membership within the three seasonal color patterns to evaluate to macroscale synchrony between river color and flow (Figure S11).

We identified four types of long-term patterns based on Mann-Kendall nonparametric trend tests ($\alpha < 0.1$) and the variability in the time series. We restricted trend analysis to rivers with more than 15 years of data between 1984 and 2018, where each year must have >5 observations spread across at least two different seasons including 83% (29,198) of reaches. Increasing λ_d is referred to as red-shifted while decreasing λ_d is referred to as blue-shifted. However, note that a significant trend only shows that color is moving toward the green/blue or yellow/red ends of the spectrum. Rivers with no significant trends were then classified as steady or variable in color. Using the full-time series, steady patterns were defined by a λ_d coefficient of variation (CV) of 1% or less and variable patterns by a λ_d CV of greater than 1%. We then identified rivers that are rapidly changing, or hotspots, by ranking the rates of change and selecting the highest 10% of rates (i.e., 90–100 percentiles). To identify local drivers, we calculated the distance between reaches with significant trends and the nearest dam (upstream or downstream) using the National Anthropogenic Barrier Database

(Ostroff, 2012), and identified if the reach overlapped with boundaries of urban areas defined by the US census (Ratcliffe et al., 2016). All analyses in Section 2.3 were conducted in R statistical software version 3.6.1 (R Core Team, 2019).

3. Results

3.1. The Most Common Color of Rivers

The primary λ_d mode was 575 nm, and 56% of all λ_d observations were yellow (Figures 1b, 1c, and 1e). The secondary λ_d mode was 497 nm, and 38% of all λ_d observations were green. Only 6% of λ_d observations were blue. Lakes caused major discontinuities in color along rivers (e.g., the Missouri and Colorado Rivers) and were blue-shifted compared to upstream and downstream rivers (Figures 1b and 1c). Separating the λ_d distribution into rivers and lakes revealed that the secondary λ_d peak was largely due to connected lakes (Figure 1f). While rivers with high mean R_s were typically yellow, likely from high suspended sediment concentrations, there was no consistent relationship between λ_d and R_s showing that λ_d provides additional information that is not contained within raw R_s (Figures 1a and S12).

The modal river color also varied regionally (Figures 1a–1c). Rivers draining the Rocky Mountains and the lower Mississippi River were red-shifted (regional mean λ_d ranged from 563 to 565 nm, Figures 1a, 1b, and S13). Rivers across much of the eastern USA (e.g., Ohio Basin, Upper Mississippi Basin) and southeastern USA were blue-shifted on average (regional mean λ_d ranged from 541 to 558 nm). Rivers in the northwestern USA (regional mean λ_d ranged from 531 to 540 nm) and northeastern USA (regional mean $\lambda_d = 522$ nm) were also blue-shifted on average.

3.2. Seasonality in River Color

We identified three dominant seasonal patterns referred to as spring red-shift (33%, 19,653 km), summer red-shift (60%, 35,297 km), and aseasonal (7%, 4,194 km). Peaks occurred 3–4 months earlier for spring red-shift compared to summer red-shift patterns (Figure 2b). In all three groups, the annual flow peak was associated with red-shifted λ_d peaks, and annual low flows were generally associated with blue-shifted λ_d troughs (summer red-shift = 173 gauges, spring red-shift = 219 gauges, and aseasonal = 40 gauges). Summer red-shift was more common in the western USA, likely driven by snowmelt driven flow and sediment pulses (Figure 2a). Spring red-shift was more common in the eastern USA. Aseasonal patterns were uncommon, and upon inspection, occurred in rivers where color varied within a narrow range or was highly variable.

3.3. Long-Term Trends

Over the full record, 33% of rivers had significant trends in color, but the direction of the trend varied regionally (Figure 3a). Twenty-one percent of rivers (18,715 km) had a decreasing trend (blue-shifted) in mean annual λ_d, which were more common in the western USA. Rates of decreasing λ_d, or the Sen's slope calculated by the Mann-Kendall test (Sen, 1968), ranged from −0.02 to −3.7 nm yr^{-1} with a mean of −0.37 nm yr^{-1}. Twelve percent of rivers (11,068 km) had a significant increasing trend (red-shifted) in mean annual λ_d, which was generally more common in the eastern USA. Rates of increasing λ_d ranged from 0.016 to 2.9 nm yr^{-1} with a mean of 0.32 nm yr^{-1}.

Most rivers did not have significant long-term trends in color (Figure 3a). Rivers with variable color over time (Figure 3c), but no trend, were common across the USA, totaling 55% of rivers (49,734 km). Twelve percent of rivers (11,191 km) had no trend and steady color over time (Figure 3d). Steady patterns were found largely in the central USA and Lower Mississippi River. We identified 534 blue-shifted hotspots located largely in the northwestern USA accounting for 40% of blue-shifted hotspots (Figures 3b and S14). However, the fastest blue-shifted rates occurred in the southern Great Plains (Figures 3b and S14). We identified 307 red-shifted hotspots located largely in the northeastern USA (22% of red-shifted hotspots) and Ohio River Basin (20% of red-shifted hotspots); however, the fastest red-shifted rates occurred in the lower Colorado River Basin (Figures 3b and S14).

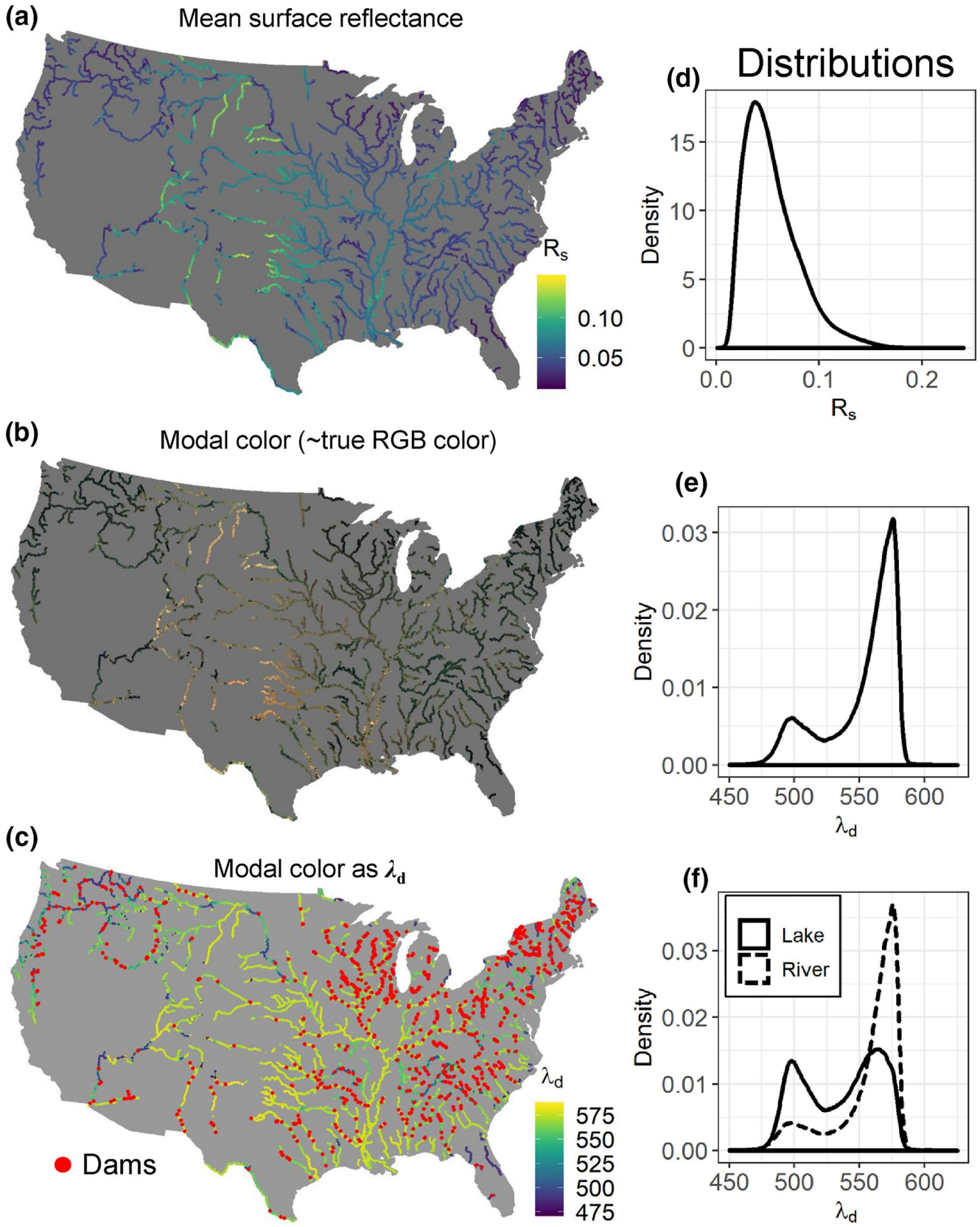
(a)
Mean surface reflectance
R_s
0.10
0.05
(b)
Modal color (~true RGB color)
(c)
Modal color as λ_d
λ_d
575
550
525
500
475
Dams
(d)
Distributions
Density
15
10
5
0
0.0
0.1
0.2
R_s
(e)
0.03
0.02
0.01
0.00
Density
450
500
550
600
λ_d
(f)
Lake
River
0.03
0.02
0.01
0.00
Density
450
500
550
600
λ_d

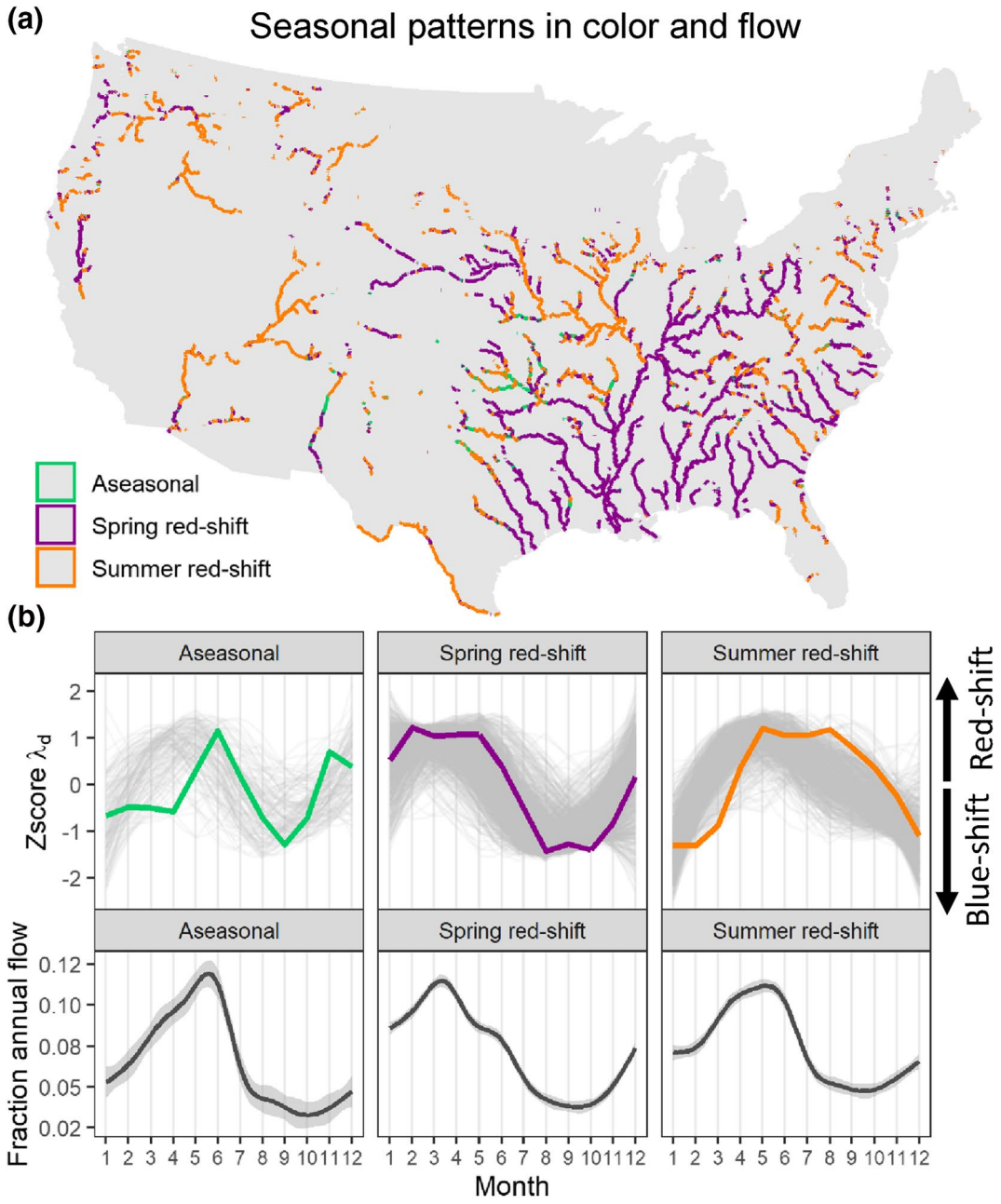

Figure 2. (a) Mapping seasonal patterns in river color defined by cluster analysis. (b) Upper row: Long-term river color regimes displaying the *z*-normalized, centroid curve plotted on top of a random sample of 10% of river reaches (for visual clarity) belonging to each seasonal pattern in gray. Lower row: Long-term flow regime across gauges located on rivers with different seasonal patterns in river color, displaying the smoothed median fraction of annual flow. Note, aseasonal, spring-red-shift, and summer-red shift refer only to river color patterns not the river flow patterns. For interactive data visualization please see, https://cuahsi.shinyapps.io/RiverColor/.

Figure 1. (a) Long-term mean R_s (blue + red + green + nir/4) averaged over each reach. (b) The most common, or modal, color as the human eye would see it from space visualized in RGB color space using hexadecimal colors, similar to a true color image. This is for visualization and is not a quantitative measurement. (c) The modal color of rivers expressed as λ_d (nm); note the color bar does not map to the actual color on the visible spectrum. Red dots are dams in the National Anthropogenic Barrier Database (Ostroff, 2012). (d) Mean R_s distribution over full RiverSR (>15.9 million measurements). (e) λ_d distribution over the full RiverSR. (f) λ_d distribution over full RiverSR separated by waterbody type, river versus lake. For interactive data visualization please see, https://cuahsi.shinyapps.io/RiverColor.

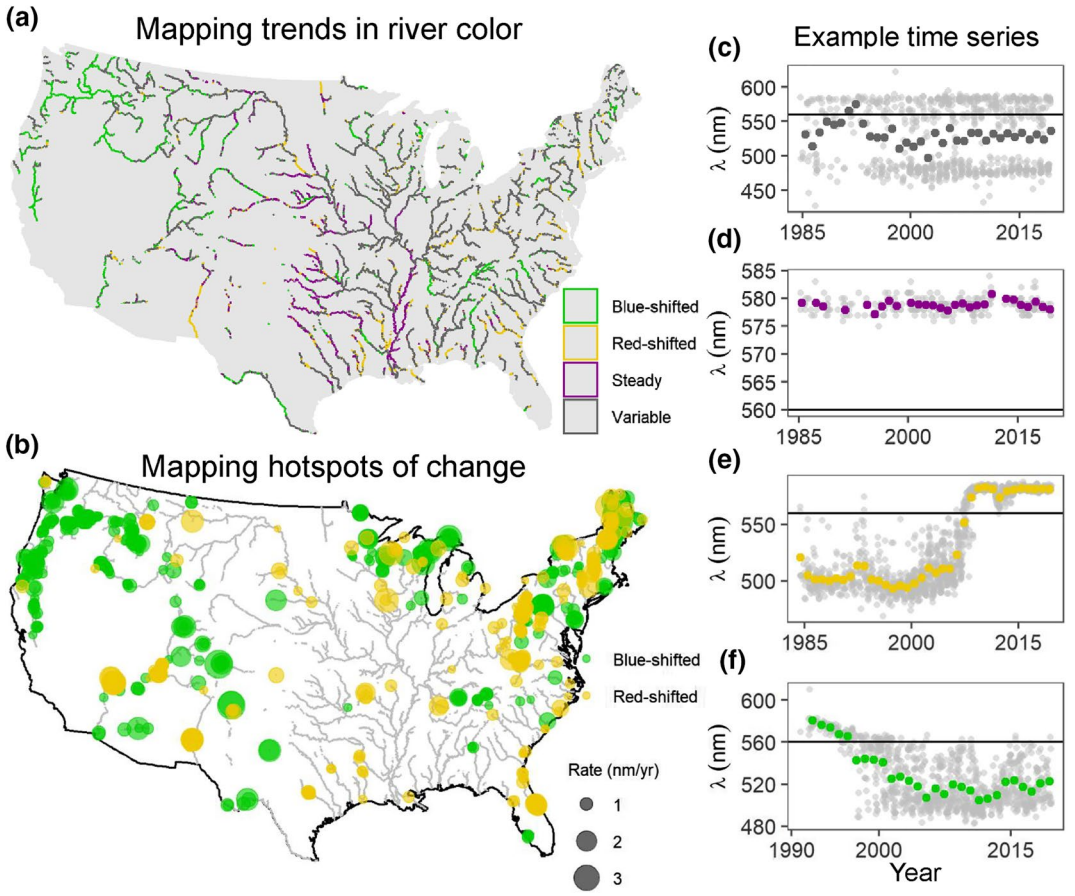

Figure 3. (a) Spatial distribution of long-term trends in river color (λ_d). (b) Spatial distribution of blue-shifted ($n = 534$) and red-shifted ($n = 307$) hotspots of change. Circle size is proportional to the rate (range: 1–3.67 nm yr^{-1}). (c) Gray smaller dots represent all observations while larger colored dots represent annual means in (c–f). Example of variable color (Colorado River, NV). (d) Example of steady color (Canadian River, OK). (e) Example of red-shifted trend (Colorado River, AZ, upstream end of Lake Mead). (f) Example of blue-shifted trend (Double Mountain Fork Brazos River, TX). The horizontal lines on plot (c–f) indicate the 560 nm boundary between yellow and green. For interactive data visualization please see, https://cuahsi.shinyapps.io/RiverColor.

4. Discussion

Our initial analysis of RiverSR focused on water color, as perceived by humans, and reveals spatial patterns and temporal trends from 1984 to 2018 in large US rivers. RiverSR has many potential applications for trend detection, identifying local impacts on water quality, and when combined with empirical or semi-analytical models, mapping water quality constituents. Here, we focus on potential drivers of river color patterns and how remote sensing of water color could advance macrosystems ecology in rivers.

4.1. Drivers of River Color

Regional and along-river variability in river color suggest both in-channel and landscape drivers of modal river color. Connected lakes and reservoirs can be sediment traps (Brune, 1953; Vörösmarty et al., 2003) and algal incubators (Soballe & Kimmel, 1987) consistent with our observations that lakes were blue-shifted (i.e., greener) and rivers were red-shifted (i.e., yellower) (Figure 1). Rivers of the southern Great Plains show the effect of both landscapes and lakes (Figure 1a). Flowing from West (semi-arid) to East (humid) across aridity, soil, and vegetation gradients (Seager et al., 2018), the red-shifted color signature of upstream landscapes was erased as sediments settled in river corridors, perhaps within successive dams (Figure 1b), and blue-shifted colors emerged. While regional climatic and landscape properties likely control the range

of colors a river can be, in-channel effects such as dams and rapid landscape transitions can reset the color of rivers. Fragmentation and transitions in color along rivers are important because color is likely linked to ecological function. The observed spatial patterns in color may be indicative of primary productivity regimes, suspended sediment, as well as light availability for photodegradation (J. P. Julian et al., 2013).

The prevalence of blue-shifted trends in the western USA and red-shifted trends in the eastern USA suggest there are regional drivers of long-term trends, including changes in hydroclimate (e.g., river flow), land use, and watershed management (J. Murphy & Sprague, 2019; Stets et al., 2020). However, we hypothesize that local drivers are also important, especially in rivers that are hotspots of change. Among rivers within the top 25 percentile of rates (e.g., fastest rates of change), 45% are near a dam (i.e., within 25 km upstream or downstream) and 22% are located within urban areas. However, among rivers within the bottom 25 percentile of rates (e.g., slowest rates of change), only 12% are near a dam and 7% within urban areas (Figure S15). To highlight examples of rapid change, water levels in Lake Mead on the Colorado River have declined since the early 2000s (Udall & Overpeck, 2017), which we observed as a shift in water color due to shrinking reservoir extent. The upstream end of the reservoir dried down transitioning from blue/green open water into a yellower river (Figure 3e). The reverse transition occurred on the Double Mountain Fork Brazos River in Texas. A dam was built in 1993 transforming a yellow river into a blue/green reservoir (Figure 3f).

4.2. Implications

Remote sensing of water color may offer new ways of quantifying seasonality in rivers that is complementary to efforts focused on measuring ecosystem processes, such as gross primary productivity (Bernhardt et al., 2018). With more validation, river color can be used as a potential proxy for ecosystem processes. River color could also provide a critical data layer for aquatic species distribution models for organisms that are sensitive to environmental conditions such as turbidity. Species distribution models typically use terrestrial landscape properties or hydrologic models rather than direct measurements of surface water, such as color (McGarvey et al., 2018; Rodriguez-Rey et al., 2019).

Trend analysis can be used to identify hotspots of change, target rivers for future experiments, and disentangle drivers of change. Limited gauge data has shown many rivers around the world have long-term trends in suspended sediment, CDOM, or chl-*a* concentrations due to both local and global drivers (Haaland et al., 2010; Li et al., 2020; J. C. Murphy, 2020; Roulet & Moore, 2006). Water color is directly measured by satellites, unlike specific water quality constituents, allowing rapid monitoring of water quality in the absence of in-situ observations.

5. Conclusions

Using a satellite remote sensing database of surface reflectance (RiverSR, available in Zenodo), we identified three dominant seasonal patterns in river color that were synchronous with long-term flow regimes, revealed that one third of large US rivers have significant shifts in color, and found evidence that hotspots of change are often located near dams and urban areas. Water color, as perceived by the human eye, is an integrative measure of water quality. It can be scaled to rivers globally and measured across multiple sensor platforms from human eyes (Garaba et al., 2015) to cell phone cameras (Leeuw & Boss, 2018; Malthus et al., 2020) to satellites. The intuitive and easily observable nature of water color could enable collection of massive volumes of data across spatial and temporal scales for water quality monitoring, identifying global hotspots of change, and advancing macrosystems ecology in rivers.

Data Availability Statement

The RiverSR (River Surface Reflectance) database for the contiguous USA and the modified NHDplusV2 flowlines to which reflectance can be joined are available on Zenodo (https://doi.org/10.5281/zenodo.4304567). Code used to generate this database can be found on Zenodo (https://doi.org/10.5281/zenodo.3839000). All other code used in analysis and figure making for this paper are available at

https://github.com/johngardner87/RiverColor. All data used to generate this database and conduct analysis presented in this paper are public including Landsat, but accessed via Google Earth Engine (https://www.usgs.gov/land-resources/nli/landsat/landsat-collection-1?qt-science_support_page_related_con=1#qt-science_support_page_related_con) NHDPlusV2 (https://www.epa.gov/waterdata/nhdplus-national-hydrography-dataset-plus), GRWL (https://zenodo.org/record/1297434#.XsbDJGhKiUk)MERIT DEM (http://hydro.iis.u-tokyo.ac.jp/%3Cyamadai/MERIT_DEM/)NABD (https://www.sciencebase.gov/catalog/item/56a7f9dce4b0b28f1184dabd).

Acknowledgments
Thank you to members of the Global Hydrology Lab at University of North Carolina-Chapel Hill, and to Phil Savoy for discussion on dynamic time warping. J. R. Gardner was supported by NSF-EAR Postdoctoral Fellowship #1806983, S. N. Topp was supported by NASA NESSF grant 80NSSC18K1398. For interactive data visualization please see, https://cuahsi.shinyapps.io/RiverColor.

References

Allen, G. H., & Pavelsky, T. M. (2018). Global extent of rivers and streams. *Science*, *361*(6402), 585–588.
Allen, G. H., Yang, X., Gardner, J., Holliman, J., David, C. H., & Ross, M. (2020). Timing of Landsat overpasses effectively captures flow conditions of large rivers. *Remote Sensing*, *12*(9), 1510.
Arbelaitz, O., Gurrutxaga, I., Muguerza, J., PéRez, J. M., & Perona, I. (2013). An extensive comparative study of cluster validity indices. *Pattern Recognition*, *46*(1), 243–256.
Bernhardt, E. S., Heffernan, J. B., Grimm, N. B., Stanley, E. H., Harvey, J., Arroita, M., et al. (2018). The metabolic regimes of flowing waters. *Limnology and Oceanography*, *63*(S1), S99–S118. https://doi.org/10.1002/lno.10726
Best, J. (2019). Anthropogenic stresses on the world's big rivers. *Nature Geoscience*, *12*(1), 7–21.
Brezonik, P., Menken, K. D., & Bauer, M. (2005). Landsat-based remote sensing of lake water quality characteristics, including chlorophyll and colored dissolved organic matter (CDOM). *Lake and Reservoir Management*, *21*(4), 373–382.
Brune, G. M. (1953). Trap efficiency of reservoirs. *Eos, Transactions American Geophysical Union*, *34*(3), 407–418.
Butman, D., & Raymond, P. A. (2011). Significant efflux of carbon dioxide from streams and rivers in the United States. *Nature Geoscience*, *4*(12), 839–842.
Carpenter, D., & Carpenter, S. (1983). Modeling inland water quality using Landsat data. *Remote Sensing of Environment*, *13*(4), 345–352.
Claverie, M., Vermote, E. F., Franch, B., & Masek, J. G. (2015). Evaluation of the Landsat-5 TM and Landsat-7 ETM+ surface reflectance products. *Remote Sensing of Environment*, *169*, 390–403.
Cory, R. M., Ward, C. P., Crump, B. C., & Kling, G. W. (2014). Sunlight controls water column processing of carbon in arctic fresh waters. *Science*, *345*(6199), 925–928.
Davies-Colley, R. J., Vant, W. N., & Smith, D. G. (2003). *Colour and clarity of natural waters*. Blackburn Press.
Davies-Colley, R. J., & Close, M. E. (1990). Water colour and clarity of New Zealand rivers under baseflow conditions. *New Zealand Journal of Marine and Freshwater Research*, *24*(3), 357–365.
Foga, S., Scaramuzza, P. L., Guo, S., Zhu, Z., Dilley, R. D., Jr, Beckmann, T., et al. (2017). Cloud detection algorithm comparison and validation for operational Landsat data products. *Remote Sensing of Environment*, *194*, 379–390.
Foley, J. A., DeFries, R., Asner, G. P., Barford, C., Bonan, G., Carpenter, S. R., et al. (2005). Global consequences of land use. *Science*, *309*(5734), 570–574.
Forel, F. (1895). *Le Léman, Monographie Limnologique II*. Lausanne, Switzerland: Librairie de l'Université.
Frasson, R. P. d. M., Pavelsky, T. M., Fonstad, M. A., Durand, M. T., Allen, G. H., Schumann, G., et al. (2019). Global relationships between river width, slope, catchment area, meander wavelength, sinuosity, and discharge. *Geophysical Research Letters*, *46*(6), 3252–3262. https://doi.org/10.1029/2019gl082027
Fuller, M. R., Doyle, M. W., & Strayer, D. L. (2015). Causes and consequences of habitat fragmentation in river networks. *Annals of the New York Academy of Sciences*, *1355*(1), 31–51.
Garaba, S. P., Friedrichs, A., Voß, D., & Zielinski, O. (2015). Classifying natural waters with the Forel-Ule colour index system: Results, applications, correlations and crowdsourcing. *International Journal of Environmental Research and Public Health*, *12*(12), 16096–16109.
Gardner, J. R., Pavelsky, T. M., & Doyle, M. W. (2019). The abundance, size, and spacing of lakes and reservoirs connected to river networks. *Geophysical Research Letters*, *46*(5), 2592–2601. https://doi.org/10.1029/2018gl080841
Giardino, C., Kõks, K.-L., Bolpagni, R., Luciani, G., Candiani, G., Lehmann, M. K., et al. (2019). The color of water from space: A case study for Italian lakes from Sentinel-2. In A. Pepe & Q. Zhao (Eds.), *Geospatial analyses of Earth Observation (EO) data* (pp. 1–14). IntechOpen.
Giardino, C., Pepe, M., Brivio, P. A., Ghezzi, P., & Zilioli, E. (2001). Detecting chlorophyll, Secchi disk depth and surface temperature in a sub-alpine lake using Landsat imagery. *Science of The Total Environment*, *268*(1–3), 19–29.
Gorelick, N., Hancher, M., Dixon, M., Ilyushchenko, S., Thau, D., & Moore, R. (2017). Google Earth Engine: Planetary-scale geospatial analysis for everyone. *Remote Sensing of Environment*, *202*, 18–27.
Griffin, C., McClelland, J., Frey, K., Fiske, G., & Holmes, R. (2018). Quantifying CDOM and DOC in major Arctic rivers during ice-free conditions using Landsat TM and ETM+ data. *Remote Sensing of Environment*, *209*, 395–409.
Grill, G., Lehner, B., Thieme, M., Geenen, B., Tickner, D., Antonelli, F., et al. (2019). Mapping the world's free-flowing rivers. *Nature*, *569*(7755), 215.
Haaland, S., Hongve, D., Laudon, H., Riise, G., & Vogt, R. (2010). Quantifying the drivers of the increasing colored organic matter in boreal surface waters. *Environmental Science & Technology*, *44*(8), 2975–2980.
Hedley, J., Harborne, A., & Mumby, P. (2005). Simple and robust removal of sun glint for mapping shallow-water benthos. *International Journal of Remote Sensing*, *26*(10), 2107–2112.
Heffernan, J. B., Soranno, P. A., Angilletta, M. J., Jr, Buckley, L. B., Gruner, D. S., Keitt, T. H., et al. (2014). Macrosystems ecology: Understanding ecological patterns and processes at continental scales. *Frontiers in Ecology and the Environment*, *12*(1), 5–14.
Hill, R. A., Weber, M. H., Debbout, R. M., Leibowitz, S. G., & Olsen, A. R. (2018). The Lake-Catchment (LakeCat) Dataset: Characterizing landscape features for lake basins within the conterminous USA. *Freshwater Science*, *37*(2), 208–221.
Hunt, R. W. G., & Pointer, M. R. (2011). *Measuring colour*. John Wiley & Sons.
Hutchinson, G. E. (1957). A Treatise on. *Limnology*, *1*, 243.
Jones, J. W. (2015). Efficient wetland surface water detection and monitoring via landsat: Comparison with in situ data from the everglades depth estimation network. *Remote Sensing*, *7*(9), 12503–12538.

Jones, J. W. (2019). Improved automated detection of subpixel-scale inundation –Revised Dynamic Surface Water Extent (DSWE) partial surface water tests. *Remote Sensing*, *11*(4), 374.
Julian, J. P., Davies-Colley, R. J., Gallegos, C. L., & Tran, T. V. (2013). Optical water quality of inland waters: A landscape perspective. *Annals of the Association of American Geographers*, *103*(2), 309–318.
Julian, J. P., Doyle, M. W., Powers, S. M., Stanley, E. H., & Riggsbee, J. A. (2008). Optical water quality in rivers. *Water Resources Research*, *44*(10). https://doi.org/10.1029/2007wr006457
Kuhn, C., de Matos Valerio, A., Ward, N., Loken, L., Sawakuchi, H. O., Kampel, M., et al. (2019). Performance of Landsat-8 and Sentinel-2 surface reflectance products for river remote sensing retrievals of chlorophyll-a and turbidity. *Remote Sensing of Environment*, *224*, 104–118.
Leeuw, T., & Boss, E. (2018). The HydroColor app: Above water measurements of remote sensing reflectance and turbidity using a smartphone camera. *Sensors*, *18*(1), 256.
Lehmann, M. K., Nguyen, U., Allan, M., & Van der Woerd, H. J. (2018). Colour classification of 1486 lakes across a wide range of optical water types. *Remote Sensing*, *10*(8), 1273.
Li, L., Ni, J., Chang, F., Yue, Y., Frolova, N., Magritsky, D., et al. (2020). Global trends in water and sediment fluxes of the world's large rivers. *Science Bulletin*, *65*(1), 62–69.
Malthus, T. J., Ohmsen, R., & Woerd, H. J. (2020). An evaluation of citizen science smartphone apps for inland water quality assessment. *Remote Sensing*, *12*(10), 1578.
McCluney, K. E., Poff, N. L., Palmer, M. A., Thorp, J. H., Poole, G. C., Williams, B. S., et al. (2014). Riverine macrosystems ecology: Sensitivity, resistance, and resilience of whole river basins with human alterations. *Frontiers in Ecology and the Environment*, *12*(1), 48–58.
McGarvey, D. J., Menon, M., Woods, T., Tassone, S., Reese, J., Vergamini, M., & Kellogg, E. (2018). On the use of climate covariates in aquatic species distribution models: Are we at risk of throwing out the baby with the bath water? *Ecography*, *41*(4), 695–712.
Mertes, L. A., Smith, M. O., & Adams, J. B. (1993). Estimating suspended sediment concentrations in surface waters of the Amazon River wetlands from Landsat images. *Remote Sensing of Environment*, *43*(3), 281–301.
Meybeck, M., Chapman, D. V., & Helmer, R. (1990). *Global freshwater quality: A first assessment*. Basil Blackwell.
Moore, R. B., & Dewald, T. G. (2016). The Road to NHDPlus – Advancements in digital stream networks and associated catchments. *JAWRA Journal of the American Water Resources Association*, *52*(4), 890–900.
Mouw, C. B., Greb, S., Aurin, D., DiGiacomo, P. M., Lee, Z., Twardowski, M., et al. (2015). Aquatic color radiometry remote sensing of coastal and inland waters: Challenges and recommendations for future satellite missions. *Remote Sensing of Environment*, *160*, 15–30.
Murphy, J. C. (2020). Declining suspended sediment in United States rivers and streams: Linking sediment trends to changes in land use/cover, hydrology and climate. *Hydrology and Earth System Sciences*, *24*(2), 991–1010. https://doi.org/10.5194/hess-24-991-2020
Murphy, J., & Sprague, L. (2019). Water-quality trends in US rivers: Exploring effects from streamflow trends and changes in watershed management. *Science of The Total Environment*, *656*, 645–658.
Nilsson, C., Reidy, C. A., Dynesius, M., & Revenga, C. (2005). Fragmentation and flow regulation of the world's large river systems. *Science*, *308*(5720), 405–408.
Olmanson, L. G., Bauer, M. E., & Brezonik, P. L. (2008). A 20-year Landsat water clarity census of Minnesota's 10,000 lakes. *Remote Sensing of Environment*, *112*(11), 4086–4097.
Ostroff, A., Wieferich, D., Cooper, A., & Infante, D. (2012). *USGS Aquatic GAP Program*. National Anthropogenic Barrier Dataset (NABD). Denver, CO: U.S. Geological Survey - Aquatic GAP Program.
Pahlevan, N., Balasubramanian, S. V., Sarkar, S., & Franz, B. A. (2018). Toward long-term aquatic science products from heritage Landsat missions. *Remote Sensing*, *10*(9), 1337.
Palmer, S. C. J., Kutser, T., & Hunter, P. D. (2015). Remote sensing of inland waters: Challenges, progress and future directions. *Remote Sensing of Environment*. *157*, 1–8. https://doi.org/10.1016/j.rse.2014.09.021
Pekel, J.-F., Cottam, A., Gorelick, N., & Belward, A. S. (2016). High-resolution mapping of global surface water and its long-term changes. *Nature*, *540*(7633), 418.
Pitarch, J., van der Woerd, H. J., Brewin, R. J., & Zielinski, O. (2019). Optical properties of Forel-Ule water types deduced from 15 years of global satellite ocean color observations. *Remote Sensing of Environment*, *231*, 111249.
Poole, G. C. (2002). Fluvial landscape ecology: Addressing uniqueness within the river discontinuum. *Freshwater Biology*, *47*(4), 641–660.
Ratcliffe, M., Burd, C., Holder, K., & Fields, A. (2016). Defining rural at the US Census Bureau. *American Community Survey and Geography Brief*, *1*(8).
Ritchie, J. C., & Cooper, C. M. (1988). Comparison of measured suspended sediment concentrations with suspended sediment concentrations estimated from Landsat MSS data. *Remote Sensing*, *9*(3), 379–387.
Ritchie, J. C., Zimba, P. V., & Everitt, J. H. (2003). Remote sensing techniques to assess water quality. *Photogrammetric Engineering & Remote Sensing*, *69*(6), 695–704.
Rodriguez-Rey, M., Consuegra, S., Börger, L., & Garcia de Leaniz, C. (2019). Improving species distribution modelling of freshwater invasive species for management applications. *PLoS One*, *14*(6), e0217896. https://doi.org/10.1371/journal.pone.0217896
Ross, M. R., Topp, S. N., Appling, A. P., Yang, X., Kuhn, C., Butman, D., et al. (2019). AquaSat: A data set to enable remote sensing of water quality for inland waters. *Water Resources Research*, *55*(11), 10012–10025.
Roulet, N., & Moore, T. R. (2006). Browning the waters. *Nature*, *444*(7117), 283–284.
Roy, D. P., Kovalskyy, V., Zhang, H., Vermote, E. F., Yan, L., Kumar, S., & Egorov, A. (2016). Characterization of Landsat-7 to Landsat-8 reflective wavelength and normalized difference vegetation index continuity. *Remote Sensing of Environment*, *185*, 57–70.
Sarda-Espinosa, A., Sarda, M. A., & LazyData, T. (2019). *Package 'dtwclust'*. Retrieved from The Comprehensive R Archive Network; https://cran.r-project.org/web/packages/dtwclust/dtwclust.pdf
Savoy, P., Appling, A. P., Heffernan, J. B., Stets, E. G., Read, J. S., Harvey, J. W., & Bernhardt, E. S. (2019). Metabolic rhythms in flowing waters: An approach for classifying river productivity regimes. *Limnology and Oceanography*, *64*(5), 1835–1851. https://doi.org/10.1002/lno.11154
Schmidt, G., Jenkerson, C., Masek, J. G., Vermote, E., & Gao, F. (2013). *Landsat Ecosystem Disturbance Adaptive Processing System (LEDAPS) Algorithm Description*, Open-File Report, 2013-1057, Reston, VA: U.S. Geological Survey. https://pubs.er.usgs.gov/publication/ofr20131057
Scott, D. T., Gomez-Velez, J. D., Jones, C. N., & Harvey, J. W. (2019). Floodplain inundation spectrum across the United States. *Nature Communications*, *10*(1), 1–8.
Seager, R., Lis, N., Feldman, J., Ting, M., Williams, A. P., Nakamura, J., et al. (2018). Whither the 100th Meridian? The once and future physical and human geography of America's arid–humid divide. Part I: The story so far. *Earth Interactions*, *22*(5), 1–22.

Sen, P. K. (1968). Estimates of the regression coefficient based on Kendall's tau. *Journal of the American Statistical Association*, *63*(324), 1379–1389.

Smith, D. G., & Davies-Colley, R. J. (1992). Perception of water clarity and colour in terms of suitability for recreational use. *Journal of Environmental Management*, *36*(3), 225–235.

Soballe, D., & Kimmel, B. (1987). A large-scale comparison of factors influencing phytoplankton abundance in rivers, lakes, and impoundments. *Ecology*, *68*(6), 1943–1954.

Stanley, E. H., Collins, S. M., Lottig, N. R., Oliver, S. K., Webster, K. E., Cheruvelil, K. S., & Soranno, P. A. (2019). Biases in lake water quality sampling and implications for macroscale research. *Limnology and Oceanography*, *64*(4), 1572–1585. https://doi.org/10.1002/lno.11136

Stets, E. G., Sprague, L. A., Oelsner, G. P., Johnson, H. M., Murphy, J. C., Ryberg, K., et al. (2020). Landscape drivers of dynamic change in water quality of US rivers. *Environmental Science & Technology*, *54*(7), 4336–4343.

Tomsett, C., & Leyland, J. (2019). Remote sensing of river corridors: A review of current trends and future directions. *River Research and Applications*, *35*(7), 779–803.

Topp, S. N., Pavelsky, T. M., Jensen, D., Simard, M., & Ross, M. R. (2020). Research trends in the use of remote sensing for inland water quality science: Moving towards multidisciplinary applications. *Water*, *12*(1), 169.

Udall, B., & Overpeck, J. (2017). The twenty-first century Colorado River hot drought and implications for the future. *Water Resources Research*, *53*(3), 2404–2418.

Van der Woerd, H. J., & Wernand, M. R. (2018). Hue-angle product for low to medium spatial resolution optical satellite sensors. *Remote Sensing*, *10*(2), 180.

Vermote, E., Justice, C., Claverie, M., & Franch, B. (2016). Preliminary analysis of the performance of the Landsat 8/OLI land surface reflectance product. *Remote Sensing of Environment*, *185*, 46–56.

Vörösmarty, C. J., Meybeck, M., Fekete, B., Sharma, K., Green, P., & Syvitski, J. P. (2003). Anthropogenic sediment retention: Major global impact from registered river impoundments. *Global and Planetary Change*, *39*(1–2), 169–190.

Wang, S., Li, J., Shen, Q., Zhang, B., Zhang, F., & Lu, Z. (2014). MODIS-based radiometric color extraction and classification of inland water with the Forel-Ule scale: A case study of Lake Taihu. *IEEE Journal of Selected Topics in Applied Earth Observations and Remote Sensing*, *8*(2), 907–918.

Wang, S., Li, J., Zhang, B., Spyrakos, E., Tyler, A. N., Shen, Q., et al. (2018). Trophic state assessment of global inland waters using a MODIS-derived Forel-Ule index. *Remote Sensing of Environment*, *217*, 444–460.

West, A. O., Nolan, J. M., & Scott, J. T. (2016). Optical water quality and human perceptions of rivers: An ethnohydrology study. *Ecosystem Health and Sustainability*, *2*(8), e01230.

Woerd, H. J., & Wernand, M. R. (2015). True colour classification of natural waters with medium-spectral resolution satellites: SeaWiFS, MODIS, MERIS and OLCI. *Sensors*, *15*(10), 25663–25680.

Woodward, G., Gessner, M. O., Giller, P. S., Gulis, V., Hladyz, S., Lecerf, A., et al. (2012). Continental-scale effects of nutrient pollution on stream ecosystem functioning. *Science*, *336*(6087), 1438–1440.

Xue, Z., Du, P., & Feng, L. (2014). Phenology-driven land cover classification and trend analysis based on long-term remote sensing image series. *IEEE Journal of Selected Topics in Applied Earth Observations and Remote Sensing*, *7*(4), 1142–1156.

Yamazaki, D., Ikeshima, D., Sosa, J., Bates, P. D., Allen, G. H., & Pavelsky, T. M. (2019). MERIT hydro: A high-resolution global hydrography map based on latest topography dataset. *Water Resources Research*, *55*(6), 5053–5073.

Yang, X., Pavelsky, T. M., Allen, G. H., & Donchyts, G. (2019). RivWidthCloud: An automated Google Earth Engine algorithm for river width extraction from remotely sensed imagery. *IEEE Geoscience and Remote Sensing Letters*, *17*(2), 217–221.

Zheng, G., & DiGiacomo, P. M. (2017). Uncertainties and applications of satellite-derived coastal water quality products. *Progress in Oceanography*, *159*, 45–72.

Zhu, Z., Wang, S., & Woodcock, C. E. (2015). Improvement and expansion of the Fmask algorithm: Cloud, cloud shadow, and snow detection for Landsats 4–7, 8, and Sentinel 2 images. *Remote Sensing of Environment*, *159*, 269–277.